Article

Revealing the spatiotemporal complexity of the magnitude distribution and *b*-value during an earthquake sequence

Marcus Herrmann [1] ✉, Ester Piegari [1] & Warner Marzocchi [1]

The Magnitude–Frequency-Distribution (MFD) of earthquakes is typically modeled with the (tapered) Gutenberg–Richter relation. The main parameter of this relation, the *b*-value, controls the relative rate of small and large earthquakes. Resolving spatiotemporal variations of the *b*-value is critical to understanding the earthquake occurrence process and improving earthquake forecasting. However, this variation is not well understood. Here we present remarkable MFD variability during the complex 2016/17 central Italy sequence using a high-resolution earthquake catalog. Isolating seismically active volumes ('clusters') reveals that the MFD differed in nearby clusters, varied or remained constant in time depending on the cluster, and increased in *b*-value in the cluster where the largest earthquake eventually occurred. These findings suggest that the fault system's heterogeneity and complexity influence the MFD. Our findings raise the question "*b*-value of what?": interpreting and using MFD variability needs a spatiotemporal scale that is physically meaningful, like the one proposed here.

Beroza et al.[1] recently highlighted that current earthquake catalogs achieve a high level of detail that likely contains more information about earthquake occurrence, allows testing of existing hypotheses, and potentially improves earthquake forecasting. One of the main ingredients for earthquake forecasting and seismic hazard models is the Magnitude–Frequency-Distribution (MFD) of earthquakes, which carries information about the proportion between small and large earthquakes. The MFD is typically modeled with the Gutenberg–Richter (GR) relation and its *b*-value (the slope of the GR relation), which can be used to infer the occurrence rate of large earthquakes from small ones. The *b*-value is observed to vary in space and time[2–8], which is thought to be primarily related to variations of the stress state in the crust[9–11]. The *b*-value is also considered as an indicator for other conditions in the crust, which are directly or indirectly related to the stress state, such as faulting style[7,12], locked or creeping fault patches[2,4,13,14], material properties[15,16], fluid pore-pressure perturbations[3,6,17,18], and critical nucleation length[19], among others[11] (and references therein). *b*-value variations may therefore have an important role in improving our physical understanding of earthquake occurrence.

Estimating the *b*-value appears trivial in theory (after all, it is simply the rate parameter of an exponential distribution), but not in practice. Several aspects affect the ability to resolve representative *b*-value variations in earthquake catalogs, such as:

1. the quality of the data, its spatiotemporal selection, and the various ways of sampling it[4,20];
2. the sample size and available magnitude range[20–24];
3. the used magnitude scale, magnitude binning, and maximum likelihood estimator[21,22,25,26];
4. the assumption of the underlying MFD model for the upper end (unbounded, tapered, or truncated) and the detection of departures from an exponential-like GR distribution at the lower end (due to the inherent and potentially varying incompleteness)[24–28], i.e., the estimation of the magnitude of completeness, M_c, as the lower magnitude threshold.

Although this list is not exhaustive, these considerations highlight that the outcome of a *b*-value analysis highly depends on expert judgment and/or subjective choices. In fact, recent scientific studies[29,30] and

[1]Dipartimento di Scienze della Terra, dell'Ambiente e delle Risorse; Università degli Studi di Napoli 'Federico II', Naples, Italy.
✉e-mail: marcus.herrmann@unina.it

discussions[31,32] reemphasized that choices have to be specific, meaningful, and reproducible to obtain robust results that contribute to a better understanding of the underlying physical processes. It appears that this field of study requires well-defined schemes and analysis steps. Moreover, choices are critical for real-time applications that need to run automatically, e.g., for operational earthquake forecasting (OEF) purposes[33]. Assessing the influence of expert choices and various modeling ideas on the forecasting performance needs community efforts such as the Collaboratory for the Study of Earthquake Predictability (CSEP)[34,35], which tests forecasting models prospectively in a controlled environment.

Here we argue that a complex earthquake sequence with multiple ruptured fault segments can further bias the MFD and b-value analysis: If the MFD varies temporally among distinct zones of a fault system, an averaged view over the whole sequence or a smoothed view over a finite scale (either in space or time) will neglect or mask those variations and may lead to inappropriate or biased inferences. Instead, an MFD analysis may become more physically meaningful and less ambiguous when accounting for distinct seismogenic zones and their evolution during the sequence. This rationale is the subject of this study. It has already been shown that the MFD can significantly differ in adjacent but well-defined zones of induced seismicity[36]. Here we focus on a complex sequence and propose to investigate the spatiotemporal behavior of the MFD and b-value by spatially isolating the most seismogenic zones and further dividing them temporally.

We use the 2016/17 central Italy (hereafter 'CI2016') sequence as an example due to its complex tectonic structure, cascading evolution, and the availability of high-resolution catalogs. The CI2016 sequence occurred in the central Apennines, one of Italy's most seismically active areas, and was marked by a cascade of three main events[37]: the M_w6.0 (M_L6.0) Amatrice event on 24 August 2016, the M_w5.9 (M_L5.8) Visso event on 26 October 2016, and the M_w6.5 (M_L6.1) Norcia mainshock on 30 October 2016. On 18 January 2017, four M_w5.0–5.5 events followed near Campotosto[37]. These seven events have been caused by movements on southwest-dipping normal faults and they ruptured multiple fault segments, activating a complex fault system[38–43].

The CI2016 sequence is particular in that it features seismicity in a ~1 km-thick subhorizontal detachment at around 10 km depth, which intersects with and confines almost the entire normal fault system above[38,40,43–45]. Such a feature was already observed in the Apennines at a depth of 15–20 km[46], which suggested the presence of a buried subhorizontal thrust related to (the deepest part of) the Apennines build-up. It generally appears as a flat layer, and high-resolution catalogs resolved it as a slightly east-dipping, irregular structure (i.e., with locally varying depth and thickness)[38]. This feature was interpreted as a midcrustal shear zone[45], which decouples the upper and lower crust. Prior seismicity was found to mostly occur along this structure[45], suggesting that it was loaded tectonically and eventually favored the unlocking of the shallower faults through stress transfer. Partially overlapping fault fragments were identified in this structure[43].

Magnitude statistics of CI2016 have been investigated in several recent studies using different spatiotemporal scales. Montuori et al.[47] mapped the b-value on a 2-km grid using the 80 nearest events; they found that the Amatrice event originated in an area with a high b-value and subsequently reduced the b-value to the north and south, suggesting a high potential for further large events. Gulia and Wiemer[48] resolved b-value changes relative to the background b-value both in time using events within focal-mechanism-driven boxes surrounding the Amatrice and Norcia epicenters, and in space on a 2-km grid using the 250 nearest events; they found a b-value variation during the course of the sequence, in particular (i) a drop after the Amatrice event (especially in the area to the north where the Norcia mainshock occurred afterward), interpreted as a still impending large earthquake, and (ii) a b-value increase after the Norcia mainshock, interpreted as a substantially reduced chance for a further large earthquake similar to

the tectonic background rate. Garća-Hernández et al.[49] used a multiscale approach to resolve the b-value continuously in time and spatially on a grid; they also observed a "marked drop of the b-value" after the Amatrice event (resolved spatially and in depth) and a recovery of the b-value to the background level after the Norcia mainshock; they could exclude that these variations were caused by an increased M_c after the main events.

In this study, we reanalyze this sequence using a high-resolution catalog and introduce an alternative perspective for studying MFD variability—using a spatiotemporal scale that considers the 3-D distribution of recorded seismicity. A cluster analysis of the sequence using density-based algorithms lets us spatially isolate the most seismogenic zones; temporal periods are defined by the occurrence time of the largest events. We demonstrate that this approach proves beneficial in resolving the spatiotemporal variation of the MFD and b-value. For instance, we resolve what happened in the days before the largest event (Norcia) in its associated seismogenic zone. Rather than solely focusing on b-value estimates, we consider it important to exploit more information from the MFD, e.g., by assessing and comparing its exponential-like part and reporting the b-value stability as function of M_c. We show that the MFD behaves in a complex manner among the spatially isolated clusters throughout the sequence. Our findings reflect on the appropriate spatiotemporal scale to resolve the b-value and challenge existing approaches.

Results
Description of clusters

Using the high-resolution catalog of Tan et al.[50], we spatially isolated the five largest seismogenic zones (Cluster 1–5, hereafter abbreviated with C1, C2, etc.) following the procedure described in Methods. Figure 1 shows that the obtained clusters are not randomly distributed, but instead highlight the complex spatial structure of the sequence. For instance, C1 comprises seismicity in the northern part of the subhorizontal detachment, parts of the normal fault (Mt. Vettore) that ruptured during the Norcia mainshock, and this mainshock hypocenter itself. C2 represents seismicity in the southern part of the subhorizontal detachment, and C3 captures the shallow northern part of the sequence, including the Visso hypocenter. C4 and C5 relate to small-scale structures. These five clusters correspond to the largest volumes of high hypocenter density (Supplementary Fig. 1). The Amatrice event does not belong to any of the main clusters because the area around its hypocenter is devoid of earthquakes[39,40,50]. The Campotosto events were also not assigned to a main cluster.

Figure 2 shows that each cluster has a distinct temporal activity. For instance, C1 was active throughout the sequence until the Campotosto events; C2 was quiet after the Visso event until the Norcia mainshock while C3 was very active in this period. C4 and C5 were mostly active toward the end of the sequence, along with the other clusters in roughly comparable proportions. Supplementary Fig. 2 and Supplementary Note 1 summarize the cluster statistics in terms of size and ratio for each period, making it more apparent that ≳50% of the earthquakes in each period belong to a cluster. Moreover, up to two clusters were dominating each period except for the last period.

Cluster-based MFD analysis using the whole sequence

For the statistical analysis of the MFD, we follow the procedure described in Methods. Table 1 and Fig. 3 indicate differences and similarities in the MFD among the clusters. In particular, Table 1 suggests that C1, C2, and C3 have identical MFD shapes, but that the MFD of C1 and C2 are distinct from the ones of C4 and C5. There is a tendency that C1 differs from C2, although not statistically significant. Figure 3c provides more details about the MFD behavior in terms of the b-value as function of M_c. For instance, the largest clusters C1–C3 (red, blue, and green, respectively) have comparable b-values (-1.2) at their corresponding $M_c^{\text{Lilliefors}}$, but behave differently for increasing M_c:
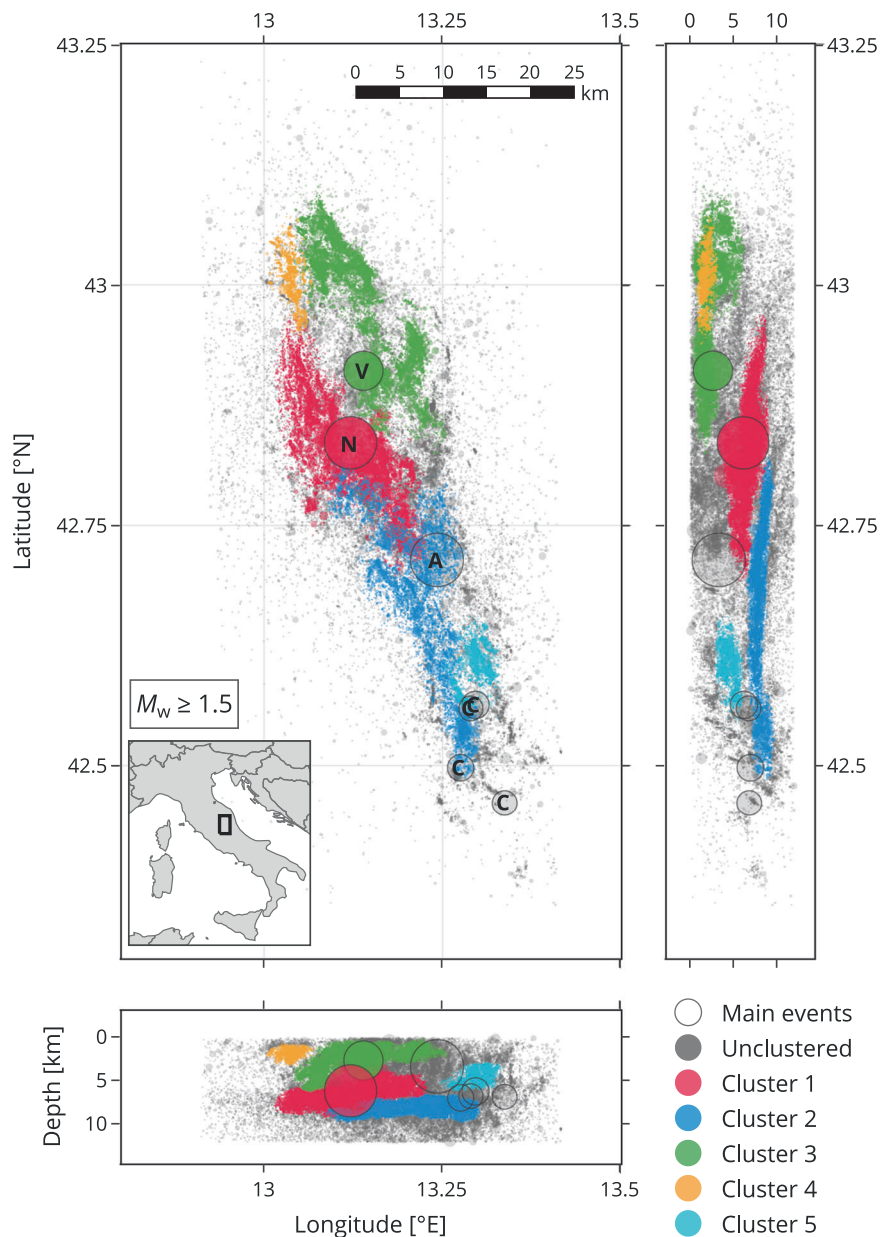
Fig. 1 | Map view and depth sections of the 2016/17 central Italy ('CI2016') seismicity with identified clusters (see legend). The depth sections are to scale. To better reveal the structure of the individual clusters, the earthquake hypocenters are plotted ascending by their cluster number on top of 'unclustered' hypocenters, neglecting a physically correct appearance. The main events Amatrice, Visso, Norcia, and four Campotosto events are represented by larger circles; in the map view, they are annotated with the respective initial letter (A, V, N, C). Supplementary Fig. 1 shows the hypocenter density for the same data.

for $M_w \geq 3.0$, the b-value is much higher in C3 than in C1 or C2. The small-scale clusters C4 and C5 (yellow and cyan, respectively) show the highest overall b-value. The Lilliefors p-value (Fig. 3b) is useful to judge the reliability of the b-value; a p-value dropping below 0.1 indicates that the b-value for C1 and C3 below $M_w 2.0$ does not relate to a persistent exponentiality with M_c, which can have several reasons (Supplementary Note 2.2) and necessitates an inspection of the MFD in individual periods, as done in the following subsection.

For the sake of completeness, we repeated the analysis using local magnitudes, M_L (Supplementary Fig. 3), which introduces a different MFD behavior for the individual clusters due to a narrower exponential range (Supplementary Note 2.3).

Cluster-based MFD analysis using temporal subsets
We extend the spatial analysis by a temporal component using three periods that exclude the short-term aftershock incompleteness (STAI)

between the main events, namely 'pre-Visso', 'pre-Norcia', and 'pre-Campotosto' (see Methods). Table 2 provides a more granular breakdown of MFD variations above $M_c^{Lilliefors}$ than Table 1, also temporally within the same cluster. For instance, in C1, only pre-Visso and pre-Norcia are distinct; in C2, no period is distinct, and in C3, pre-Visso is distinct from the other two periods. The MFD in pre-Campotosto is never distinct in any cluster. Comparisons among clusters for the same temporal period show no significant differences between C1 and C2, but when comparing C1 or C2 with C3. (Note that the sample size of C2 in pre-Norcia is very small (26 earthquakes), which reduces the power of the KS test to detect potential differences for pairs that include this subset.) The most unique subset is C3 during pre-Visso, which differs from almost all other subsets. Of all 36 pairs, 15 (42%) are significantly different.

Further investigating the MFDs in terms of a M_c-dependent b-value (Figs. 4 and 5) provides a more nuanced discrimination. The most
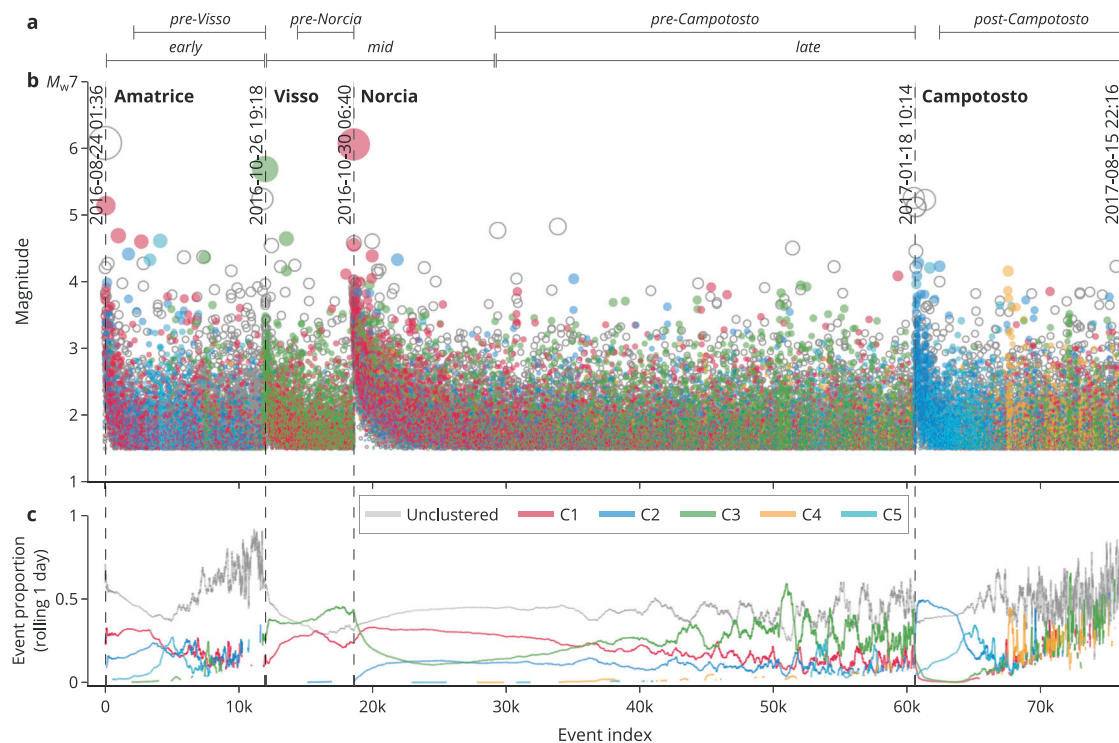
Fig. 2 | Temporal evolution of CI2016 seismicity colored by cluster association (see legend). The horizontal axis represents the index of the shown earthquakes. **a** Overview of the temporal subsets. **b** Magnitude vs. index of individual events (empty circles denote 'unclustered'); the occurrence times of main events are annotated vertically. **c** Proportion between the number of earthquakes in each cluster and the total number of earthquakes using a rolling window of the previous 24 h.

remarkable observation is that the b-value in C1 is highest before the Norcia mainshock—it has increased after the Visso event from 1.4 to 1.6. After the Norcia mainshock, the b-value remained at a high level (1.5 in the pre-Campotosto period). In C2, the b-value remained high at ~1.45 both before the Visso event and after the Norcia mainshock. (This cluster does not contain enough earthquakes in the pre-Norcia period to estimate a b-value.) In C3, which contains the Visso event, the b-value increased from 1.0 in pre-Visso to 1.4 in pre-Norcia, at which level it stayed also after the Norcia mainshock.

Figure 5 facilitates a temporal comparison of the MFD among the clusters. In pre-Visso, the b-value is similar in C1 and C2 at around 1.4, and much lower in C3 (1.0). Prior to the Norcia mainshock, the b-value increased both in C1 and C3 (to $1.4 - 1.6$); C2 does not provide enough data. After the Norcia mainshock (i.e., pre-Campotosto), the b-value remains elevated in C1–C3 ($1.3 - 1.5$) and C1 and C2 have similar b-values again. After the Campotosto events (Supplementary Fig. 8, 'post-Campotosto'), the b-value still remains elevated in C1–C3 ($1.4 - 1.5$).

For the sake of completeness, we repeated the analysis using M_L (Supplementary Figs. 4, 5, and Supplementary Note 2.3), which reproduces our main findings qualitatively with comparable relative b-value changes, albeit the b-value behaves differently as function of M_c owing to the scale change. For a comparison using temporal periods that include STAI, see Supplementary Note 2.4 and Supplementary Figs. 6–8.

Discussion

We found that the individual earthquake clusters, which represent the most active zones of this complex sequence, are characterized by a significantly different MFD behavior. In particular, the MFD experienced variations as temporal changes and spatial differences, or remained identical within one cluster throughout the sequence. Finding this complex MFD variability highlights that the spatio-temporal scale to select seismicity and resolve the b-value must be physically meaningful. In the following, we first discuss the observed temporal behavior, followed by a discussion of spatial differences and similarities, an interpretation of our findings, and a summary with implications and outlooks.

Regarding the temporal evolution, the most striking observation is the gradual b-value increase in the cluster where the strongest earthquake eventually occurred (C1). Apparently, a high b-value did not prevent the nucleation of a large rupture in this cluster. This resolved behavior differs from the general observation that the b-value decreases prior to large earthquakes[5,48,51–53], albeit similar observations to ours do exist[54]. The increasing b-value in C1 after the Visso event highlights that activity in one cluster may influence the MFD in another one. After the Visso event, the b-value also increased in its own cluster (C3), which corroborates that large earthquakes may influence the MFD in their surrounding[55]. The later Norcia mainshock, however, did not alter the MFD in the three main clusters further and the b-value remained high—also after the Campotosto events, which occurred in the southern part of the sequence. This stagnating b-value highlights that the MFD eventually became insensitive to large earthquakes even though it had experienced significant temporal variations in the same

Table 1 | Pairwise comparison of the cumulative magnitude distribution of each cluster against the others

	Cluster 1	**Cluster 2**	**Cluster 3**	**Cluster 4**	**Cluster 5**
Cluster 1		0.089	0.26	**2.2e-06**	**1.2e-06**
Cluster 2	0.089		0.59	**0.024**	**0.0084**
Cluster 3	0.26	0.59		0.49	0.36
Cluster 4	**2.2e-06**	**0.024**	0.49		0.51
Cluster 5	**1.2e-06**	**0.0084**	0.36	0.51	

p-values of two-sample Kolmogorov–Smirnov tests (Methods). Statistically significant p-values are highlighted in bold.
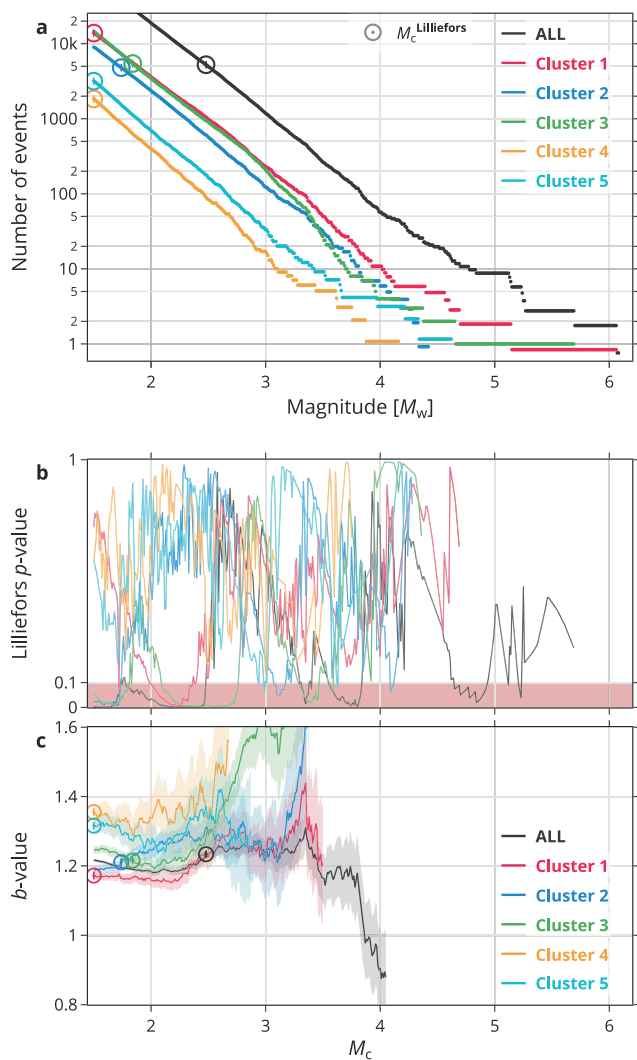
Fig. 3 | Magnitude statistics for all data (black) and individual clusters (see legend). a Representing the data in terms of their magnitude−frequency distribution (MFD). Note that a tiny value is added to each MFD (between − 0.1 and 0.1) to avoid visual overlaps at large magnitudes. **b** The Lilliefors *p*-value (assuming an exponential distribution as null hypothesis) as a function of lower magnitude cutoff, or magnitude of completeness, M_c (see Methods). **c** The estimated *b*-value (the slope of the fitted Gutenberg–Richter relation, see Methods) as a function of M_c with the shading representing 1σ. The $M_c^{\text{Lilliefors}}$ estimates are indicated for each cluster in **a** and **c** with a circle marker. Supplementary Fig. 3 shows the same analysis using local magnitudes.

seismogenic zones earlier. This ambiguous MFD character is compounded by its behavior in C2, where the MFD locally remained constant throughout the sequence—apparently unaffected by surrounding seismicity.

When comparing clusters spatially regarding the whole sequence, we found differences in the MFD between the largest clusters (C1 and C2) and the smaller ones (C4 and C5). The former have overall lower *b*-value estimates, which are due to the stronger influence of STAI as a result of their proximity to larger earthquakes. In fact, the *b*-value is underestimated in periods that include STAI (Supplementary Note 2.4 and Supplementary Figs. 7–9). Excluding STAI in the individual time periods, we found spatial MFD differences among the largest clusters (C3 differing from C1 and C2). Simultaneously, MFD similarities coexisted among these clusters (C1 and C2), although we do not have evidence for every time period, such as for pre-Norcia when C2 only provides few samples. C1 and C2 have in common that they represent

the majority of seismicity in the subhorizontal detachment at depth (its northern and southern extension, respectively). With their MFD differing from C3 in each individual period and tending toward a higher *b*-value indicates that this subhorizontal detachment is not only tectonically distinct from the shallower normal faults (see Introduction), but also in terms of the MFD.

Although our study focuses on raising awareness of appropriately resolving MFD and *b*-value variations, we briefly speculate about the underlying causes for our most remarkable observations in this sequence. The marked MFD variability among the clusters over time may reflect a heterogeneous stress field and/or a complex fault geometry with significant contributions from the subhorizontal detachment. In other words, the different spatiotemporal behavior of the elastic energy release may be related to some particular (and unknown) features of the geological setting. Moreover, a complex rupture process is suggested by the fact that only some main events belong to clusters—a result of the different hypocenter densities surrounding these events. Assuming the *b*-value is inversely related to the stress state[9,10], the generally higher *b*-value in the subhorizontal detachment could be caused by the structure's reduced capacity to accumulate stress. Instead of accumulating stress, it preferentially transfers stress to the shallow fault system, favoring its unlocking[45]. In fact, this subhorizontal thrust is known to release microearthquakes quasi-continuously along its entire length[38,56], occasionally in minor sequences[57,58], but not hosting larger earthquakes (which should have an extensional mechanism). The very high *b*-value prior and close to the hypocenter of the Norcia mainshock could be explained with (i) the generally high *b*-value in the subhorizontal detachment because C1's pre-Norcia seismicity occurred within its north-eastern extension, whereas its pre-Visso seismicity was located in a shallower part (Supplementary Fig. 10); and (ii) the previous two main events (Amatrice and Visso) and their aftershocks gradually releasing built-up strain and reducing the overall stress in the fault zone. A noteworthy side observation is that the Norcia mainshock nucleated in between the pre-Norcia and the pre-Visso subset of C1 (i.e., the aftershock zones of Amatrice and Visso, respectively, see also Improta et al.[39]), which is consistent with observations that large earthquakes tend to nucleate at the rim of seismic clouds[59,60] and the cascading stress transfer hypothesis[61,62].

In summary, our study demonstrated that the spatiotemporal isolation of seismicity clusters resolves a distinct MFD behavior among the most active zones over time, including influences between them. We therefore argue that the MFD highly depends on the observed seismogenic zone. Since the most seismogenic zones in turn govern the overall MFD behavior of a sequence, a consideration of the activity in individual clusters allows us to decompose and analyze the most important contributions of a complex sequence. Our findings highlight the delicate issue of choosing an appropriate spatiotemporal scale to resolve the *b*-value, challenging existing approaches: A too large scale merges potentially different MFD behavior in individual seismogenic zones and a too fine resolution obscures the tectonic relation and neglects the statistical robustness. The cluster-based approach presented here uses the seismicity distribution itself to choose a scale that is physically meaningful and statistically robust. This strategy may help to reduce the amount of expert judgment and subjective choices, paving the way for replicable MFD analyses and a unified interpretation of MFD and *b*-value variability. For instance, a spatial scale based on density-based clustering can provide appropriate reference volumes (e.g., to determine a background *b*-value for each zone—an analysis that we omitted only due to inconsistent moment magnitude estimates, see Methods). Besides the spatiotemporal scale, other factors and choices complicate a meaningful interpretation; we discuss several of them in Supplementary Note 2, for example MFD exponentiality, STAI, the used magnitude scale, and the used catalog. These

Table 2 | Pairwise MFD comparison of temporal subsets

	Cluster 1			Cluster 2			Cluster 3		
	(pre-V.)	(pre-N.)	(pre-C.)	(pre-V.)	(pre-N.)	(pre-C.)	(pre-V.)	(pre-N.)	(pre-C.)
C1 (pre-Visso)		**0.0037**	0.33	0.59	0.74	**0.03**	**2.1e-05**	0.86	0.79
C1 (pre-Norcia)	**0.0037**		0.23	**0.01**	0.72	**0.044**	**1.3e-09**	**0.0056**	0.052
C1 (pre-Campotosto)	0.33	0.23		0.52	0.42	0.21	**5.8e-06**	0.62	**0.013**
C2 (pre-Visso)	0.59	**0.01**	0.52		0.78	0.28	**2.5e-06**	0.51	0.068
C2 (pre-Norcia)	0.74	0.72	0.42	0.79		0.51	0.093	0.42	0.26
C2 (pre-Campotosto)	**0.03**	**0.044**	0.21	0.28	0.5		**7.6e-08**	**0.0087**	**0.018**
C3 (pre-Visso)	**2.1e-05**	**1.3e-09**	**5.8e-06**	**2.5e-06**	0.093	**7.6e-08**		**3.2e-06**	**0.012**
C3 (pre-Norcia)	0.86	**0.0056**	0.62	0.51	0.42	**0.0087**	**3.2e-06**		0.099
C3 (pre-Campotosto)	0.79	0.052	**0.013**	0.068	0.26	**0.018**	**0.012**	0.099	

Statistically significant p-values are highlighted in bold.
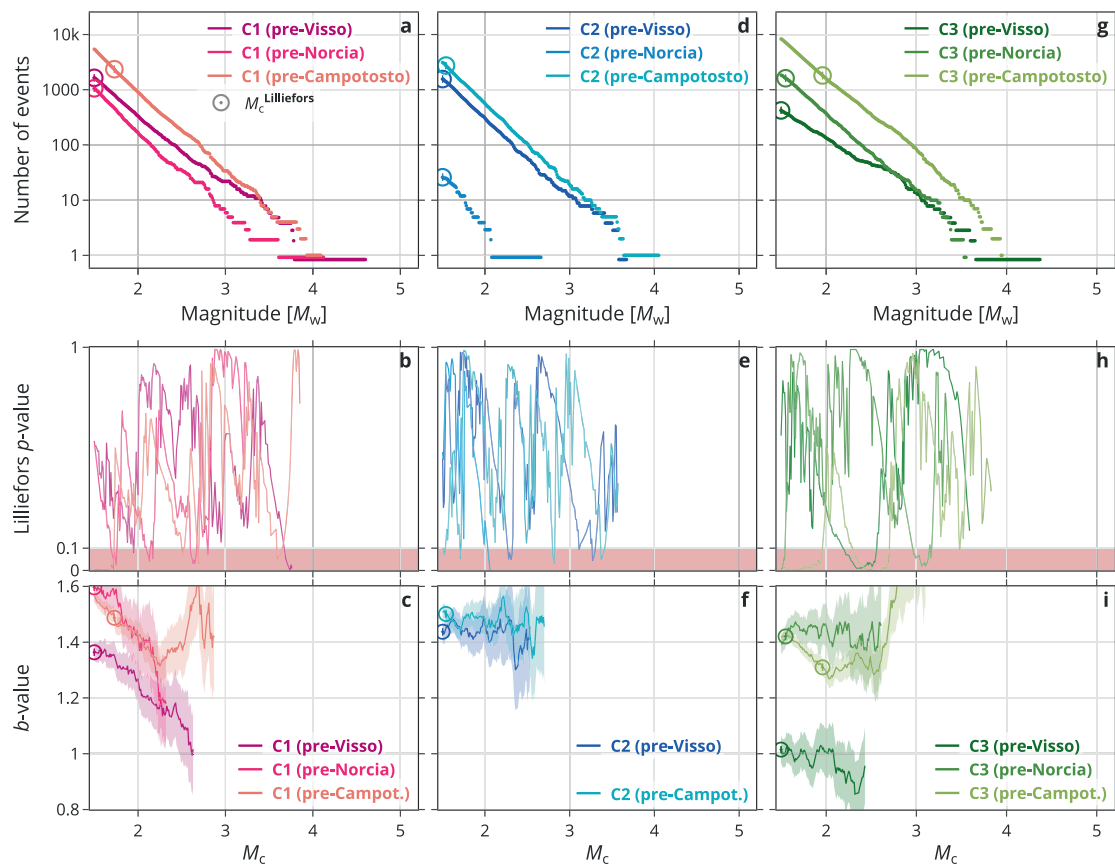Like Table 1, but for three periods of Cluster 1, 2, and 3 that exclude short-term incompleteness (STAI).

Fig. 4 | Magnitude statistics of the three largest clusters in three individual periods. a–c Cluster 1, **d–f** Cluster 2, and **g–i** Cluster 3. Like Fig. 3, **a**, **d**, and **g** show clusters in terms of their magnitude–frequency distribution; **b**, **e**, and **h** show the Lilliefors p-value as function of M_c; and **c**, **f**, and **i** the b-value as function of M_c with the shading representing 1σ. Supplementary Fig. 4 shows the same analysis using local magnitudes. Supplementary Figs. 7 and 8 compare the periods shown here with periods that include STAI.

additional aspects influence and potentially bias b-value estimates and are not always carefully addressed. We emphasize that the absolute b-value has little meaning not only due to its dependence on the magnitude scale (Supplementary Note 2.3), but also on the particular conversion relation (Supplementary Note 2.5 and Supplementary Fig. 9).

Generalizing our findings, we hypothesize that a complex and distinct MFD behavior is not unique to the CI2016 sequence, but likely occurs in other regions and sequences. In particular, our results predict that in a larger region (like the extent of the CI2016 sequence), the temporal b-value variability must exceed the expected natural

variability (i.e., uncertainty) of a constant b-value, as found in various regions[5,11,48,53]. Our method may be beneficial for studying the peculiarities of spatiotemporal MFD variability to better understand the processes that influence seismicity. For instance, it may aid in exploring and modeling stress heterogeneities to improve the earthquake forecasting skill of physics-based models[63–65]. Even if the physical processes remain hidden, merely recognizing that the MFD behaves in a complex manner potentially improves the spatiotemporal forecast performance—it is a way to better appreciate the fine-scale heterogeneity and complexity of activated tectonic structures. Future work may focus on a refined identification of spatiotemporal clusters to
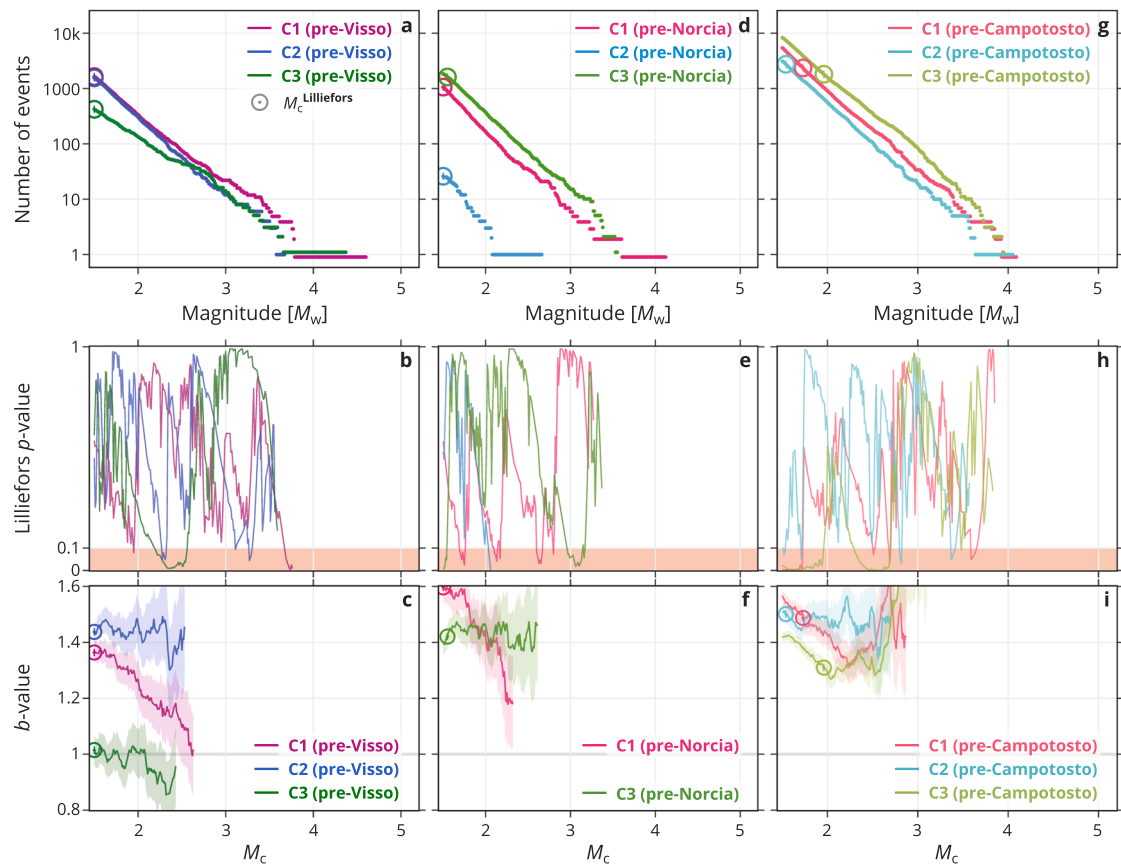
Fig. 5 | Reordering the magnitude statistics of Fig. 4 temporally by period. a–c 'pre-Visso', **d–f** 'pre-Norcia', and **g–i** 'pre-Campotosto'. Like Figs. 3 and 4, **a**, **d**, and **g** show clusters in terms of their magnitude–frequency distribution;

b, **e**, and **h** show the Lilliefors p-value as function of M_c; and **c**, **f**, and **i** the b-value as function of M_c with the shading representing 1σ. Supplementary Fig. 5 shows the same analysis using local magnitudes.

better connect them with individual tectonic structures, possibly by not relying solely on hypocenter density.

Methods

High-resolution earthquake catalog of the sequence

We used the high-resolution catalog of Tan et al.[50], which spans from 2016-08-15 to 2017-08-15, and extracted a spatial subset as follows: depth < 12 km; UTM easting: 330–370 km (about longitude 12.94–13.40); UTM northing: 4690–4790 km (about latitude 42.34–43.25). Only earthquakes with moment magnitudes $M_w \geq 1.5$ were considered, totaling 76 055 events. The provided hypocenters are based on high-precision relative relocation. The M_w contained in the catalog were converted from local magnitudes, M_L, with an average European scaling relation[66] based on a polynomial fit using catalogs of different seismological agencies with most events having $M_L > 1.5$ and $M_w \gtrsim 1.5$, but adjusted to regional data (Supplementary Note 2.3).

Identifying spatial earthquake clusters and creating temporal subsets

To infer the spatial distribution of seismogenic zones, we followed recommendations based on density-based clustering analyses of earthquake catalogs[67]. Accordingly, earthquake hypocenters were spatially separated into clusters using DBSCAN (Density-Based Spatial Clustering of Applications with Noise)[68], which groups points based on how closely they are packed together and allows identifying volumes of arbitrary shapes; points that lie in low-density zones are left as outliers. Because the horizontal extension of the CI2016 sequence is several times larger than the vertical extension, density-connected clouds of hypocenters preferentially extend in horizontal directions. To improve the clustering analysis for such an anisotropic case, we

rescaled the hypocenter coordinates to a uniform extent in each direction, i.e., rescaled into a cube. This procedure increased the local hypocenter density in horizontal planes, which facilitated identifying hypocenter clusters with horizontally elongated shapes[67] (Supplementary Fig. 1). DBSCAN was then applied with parameter values that led to an optimal clustering solution[67]: $\epsilon = 0.40$, the neighborhood radius and $Z = 200$, the minimum number of points required to form a dense region. This configuration produced nine clusters, from which we selected the five largest (C1–5, descending by size) and labeled the remaining earthquakes as 'unclustered'. Their spatial distribution is shown in Fig. 1 and the data is provided as Supplementary Data 1.

To enable a temporal analysis, each of the largest clusters C1–C3 was divided into three periods (see indicators in Fig. 2):

- early: earthquakes between the Amatrice and Visso event;
- mid: earthquakes since the Visso event until 2 days after the Norcia mainshock;
- late: the rest.C4 and C5 contain too few data to benefit from this division.

As illustrated in Supplementary Fig. 6, these periods are affected by short-term aftershock incompleteness (STAI, see also Supplementary Note 2.4)[69–72]. Supplementary Fig. 6 makes use of equalized plot scales[73] and overlays the point density as suggested by W. Ellsworth (pers. comm., 2021). In this way, Supplementary Fig. 6 informs us about the STAI duration after each main event, leading us to exclude STAI by using temporal subsets of the three periods for C1, C2, and C3 (see indicators at the top of Fig. 2):

- pre-Visso: like 'early', but excluding the first 0.8 days after the Amatrice event;
- pre-Norcia: like 'mid', but excluding the first 0.6 days after the Visso event and 2 days after the Norcia mainshock;

- pre-Campotosto: like 'late', but before the Campotosto event;
- post-Campotosto: like 'late', but after the Campotosto event excluding the first 0.4 days.

Earthquake statistics

The clusters and their temporal subsets were investigated in terms of their MFD. To quantify MFD variability, we calculated the b-value as function of M_c for each cluster or temporal subset. The b-value was determined using a bias-free maximum likelihood estimation[22,74] for sample sizes $N \geq 50$. The b-value requires an exponential distribution of the magnitude above M_c to be physically meaningful[25]. To assess the exponentiality of the MFD, we applied the Lilliefors test[25,26] using the implementation of Herrmann and Marzocchi[75] and obtain a p-value as function of M_c, which expresses the probability to observe the MFD assuming that the exponential distribution is the underlying distribution. For a significance level of $\alpha = 0.1$, we derived the lowest magnitude level for which the MFD can be considered exponential, referred to as $M_c^{\text{Lilliefors}}$. We always refer to the b-value at $M_c^{\text{Lilliefors}}$.

As an alternative to quantify MFD variability, we used the two-sample Kolmogorov–Smirnov (KS) test and compared the MFD of clusters or their temporal subsets pairwise. For each pair, the largest $M_c^{\text{Lilliefors}}$ was used as lower magnitude cutoff. The KS test returns a p-value as a measure for the strength of evidence against the null hypothesis that the two MFDs come from the same parent distribution. We interpreted a p-value < 0.05 as a statistically significant difference.

We assumed that distinct b-values or significant p-values reflect differences or changes of the entire exponential part of the MFD. This assumption is rather simplistic because both metrics are not ideal representations of the MFD: While the b-value estimate increasingly correlates with the largest magnitude for decreasing sample sizes[25], the KS test has a generally reduced sensitivity for differences toward the tails of the distributions. But they are the most widely accepted metrics available for representing the MFD or their differences. We did not explore whether the MFD could be characterized by a tapered GR distribution, and therefore neglected variations of the maximum magnitude, e.g., due to released energy close to faults[28].

Consider prior seismicity?

The high-resolution catalog of Tan et al.[50] only contains 15 events with $M_w \geq 1.5$ before the first main event (the Amatrice event). To better represent prior seismicity in the MFD analyses (e.g., as a reference "background" b-value), we initially considered HORUS[76] (horus.bo.ingv.it) as a temporally extensive catalog that provides M_w magnitudes. HORUS has already been used to study the CI2016 sequence in terms of b-value[48]. The M_w in HORUS were converted from M_L with a different scaling relation[77] than the M_w in the high-resolution catalog[66]. (Note that the M_L estimates in either catalog are also not based on the same procedure.) In fact, a comparative MFD analysis for CI2016 seismicity shows that the b-value differs considerably between both catalogs (0.2 units at $M_c^{\text{Lilliefors}}$, see Supplementary Note 2.5 and Supplementary Fig. 9). The two M_w scales are not consistent with each other, rendering a reliable MFD comparison impossible. We therefore did not use the HORUS catalog and omitted prior seismicity in our MFD analyses.

Data availability

The high-resolution earthquake catalog of Tan et al.[50] is available at Tan et al.[78]. The extracted events with their associated cluster indices obtained in this study can be found in Supplementary Data 1.

Code availability

No proprietary code was used in this study; the performed analysis can be reproduced from the specifications in the Methods section. The density-based cluster identification following the recommendations of Piegari et al.[67] is based on the DBSCAN algorithm implemented in `Matlab` (www.mathworks.com/help/stats/dbscan.html); $M_c^{\text{Lilliefors}}$ was

calculated with the Python class of Herrmann and Marzocchi[75]. Figures were created with the Python graphing library `plotly` (www.plotly.com/python).

References

1. Beroza, G. C., Segou, M. & MostafaMousavi, S. Machine learning and earthquake forecasting—next steps. *Nat. Commun.* **12**, 4761 (2021).
2. Wiemer, S. & Wyss, M. Mapping the frequency-magnitude distribution in asperities: An improved technique to calculate recurrence times? *J. Geophys. Res. Solid Earth* **102**, 15115–15128 (1997).
3. Hainzl, S. & Fischer, T. Indications for a successively triggered rupture growth underlying the 2000 earthquake swarm in Vogtland/NW Bohemia. *J. Geophys. Res. Solid Earth* **107**, ESE 5–1–ESE 5–9 (2002).
4. Tormann, T. et al. Size distribution of Parkfield's microearthquakes reflects changes in surface creep rate. *Geophys. J. Int.* **193**, 1474–1478 (2013).
5. Gulia, L., Tormann, T., Wiemer, S., Herrmann, M. & Seif, S. Short-term probabilistic earthquake risk assessment considering time-dependent b values. *Geophys. Res. Lett.* **43**, 1100–1108 (2016).
6. Shelly, D. R., Ellsworth, W. L. & Hill, D. P. Fluid-faulting evolution in high definition: Connecting fault structure and frequency-magnitude variations during the 2014 Long Valley Caldera, California, earthquake swarm. *J. Geophys. Res. Solid Earth* **121**, 1776–1795 (2016).
7. Petruccelli, A. et al. The influence of faulting style on the size-distribution of global earthquakes. *Earth Planet. Sci. Lett.* **527**, 115791 (2019).
8. Taroni, M., Zhuang, J. & Marzocchi, W. High-definition mapping of the Gutenberg-Richter b-value and its relevance: a case study in Italy. *Seismol. Res. Lett.* **92**, 3778–3784 (2021).
9. Wyss, M. Towards a physical understanding of the earthquake frequency distribution. *Geophys. J. Int.* **31**, 341–359 (1973).
10. Scholz, C. H. On the stress dependence of the earthquake b value. *Geophys. Res. Lett.* **42**, 1399–1402 (2015).
11. El-Isa, Z. H. & Eaton, D. W. Spatiotemporal variations in the b-value of earthquake magnitude-frequency distributions: Classification and causes. *Tectonophysics* **615-616**, 1–11 (2014).
12. Schorlemmer, D., Wiemer, S. & Wyss, M. Variations in earthquake-size distribution across different stress regimes. *Nature* **437**, 539–42 (2005).
13. Sobiesiak, M., Meyer, U., Schmidt, S., Götze, H.-J. & Krawczyk, C. M. Asperity generating upper crustal sources revealed by b value and isostatic residual anomaly grids in the area of Antofagasta, Chile. *J. Geophys. Res.* **112**, B12308 (2007).
14. Ghosh, A., Newman, A. V., Thomas, A. M. & Farmer, G. T. Interface locking along the subduction megathrust from b-value mapping near Nicoya Peninsula, Costa Rica. *Geophys. Res. Lett.* **35**, L01301 (2008).
15. Mogi, K. Magnitude-frequency relation for elastic shocks accompanying fractures of various materials and some related problems in earthquakes (2nd Paper). *Bull. Earthq. Res. Inst.* **40**, 831–853 (1962).
16. Goebel, T. H., Kwiatek, G., Becker, T. W., Brodsky, E. E. & Dresen, G. What allows seismic events to grow big?: Insights from b-value and fault roughness analysis in laboratory stick-slip experiments. *Geology* **45**, 815–818 (2017).
17. Bachmann, C. E., Wiemer, S., Goertz-Allmann, B. P., and Wössner, J. Influence of pore-pressure on the event-size distribution of induced earthquakes. *Geophys. Res. Lett.* https://doi.org/10.1029/2012GL051480 (2012).
18. Passarelli, L. et al. Aseismic transient driving the swarm-like seismic sequence in the Pollino range, Southern Italy. *Geophys. J. Int.* **201**, 1553–1567 (2015).

19. Dublanchet, P. Stress-dependent b value variations in a heterogeneous rate-and-state fault model. *Geophys. Res. Lett.* **47**, e2020GL087434 (2020).

20. Roberts, N. S., Bell, A. F. & Main, I. G. Mode switching in volcanic seismicity: El Hierro 2011–2013. *Geophys. Res. Lett.* **43**, 4288–4296 (2016).

21. Wiemer, S. & Wyss, M. Mapping spatial variability of the frequency-magnitude distribution of earthquakes. *Adva. Geophys.* https://doi.org/10.1016/S0065-2687(02)80007-3 (2002).

22. Marzocchi, W. & Sandri, L. A review and new insights on the estimation of the b-value and its uncertainty. *Ann. Geophysics* **46**, 1271–1282 (2003).

23. Nava, F. A., Márquez-Ramírez, V. H., Zúñiga, F. R., Ávila-Barrientos, L. & Quinteros, C. B. Gutenberg-Richter b-value maximum likelihood estimation and sample size. *J. Seismol.* **21**, 1–9 (2016).

24. Geffers, G.-M., Main, I. G. & Naylor, M. Biases in estimating b-values from small earthquake catalogues: How high are high b-values? *Geophys. J. Int.* **229**, 1840–1855 (2022).

25. Marzocchi, W., Spassiani, I., Stallone, A. & Taroni, M. How to be fooled searching for significant variations of the b-value. *Geophys. J. Int.* **220**, 1845–1856 (2020).

26. Herrmann, M. & Marzocchi, W. Inconsistencies and lurking pitfalls in the magnitude-frequency distribution of high-resolution earthquake catalogs. *Seismological Res. Lett.* **92**, 909–922 (2021).

27. Kagan, Y. Y. Seismic moment distribution revisited: I. Statistical results. *Geophys. J. Int.* **148**, 520–541 (2002).

28. Spassiani, I. & Marzocchi, W. An energy-dependent earthquake moment-frequency distribution. *Bull. Seismological Soc. Am.* **111**, 762–774 (2021).

29. Dascher-Cousineau, K., Lay, T. & Brodsky, E. E. Two Foreshock sequences post Gulia and Wiemer (2019). *Seismol. Res. Lett.* **91**, 2843–2850 (2020).

30. DeSalvio, N. D. & Rudolph, M. L. A retrospective analysis of b-value changes preceding strong earthquakes. *Seismol. Res. Lett.* **93**, 364–375 (2021).

31. Gulia, L. & Wiemer, S. Comment on 'Two foreshock sequences post Gulia and Wiemer (2019)' by Kelian Dascher-Cousineau, Thorne Lay, and Emily E. Brodsky. *Seismol. Res. Lett.* **92**, 3251–3258 (2021).

32. Dascher-Cousineau, K., Lay, T. & Brodsky, E. E. Reply to "Comment on 'Two foreshock sequences post Gulia and Wiemer (2019)' by Kelian Dascher-Cousineau, Thorne Lay, and Emily E. Brodsky" by Laura Gulia and Stefan Wiemer. *Seismol. Res. Lett.* **92**, 3259–3264 (2021).

33. Jordan, T. H. et al. Operational earthquake forecasting: State of knowledge and guidelines for utilization. *Ann. Geophys.* https://doi.org/10.4401/ag-5350 (2011).

34. Zechar, J. D. et al. The Collaboratory for the Study of Earthquake Predictability perspective on computational earthquake science. *Concurr. Comput. Pract. Exp.* **22**, 1836–1847 (2010).

35. Schorlemmer, D. et al. The Collaboratory for the Study of Earthquake Predictability: Achievements and priorities. *Seismol. Res. Lett.* **89**, 1305–1313 (2018).

36. Igonin, N., Zecevic, M. & Eaton, D. W. Bilinear magnitude-frequency distributions and characteristic earthquakes during hydraulic fracturing. *Geophys. Res. Lett.* **45**, 12,866–12,874 (2018).

37. ISIDe Working Group. *Italian Seismological Instrumental and Parametric Database (ISIDe)* https://doi.org/10.13127/ISIDE (2007).

38. Chiaraluce, L. et al. The 2016 central Italy seismic sequence: A first look at the mainshocks, aftershocks, and source models. *Seismol. Res. Lett.* **88**, 757–771 (2017).

39. Improta, L. et al. Multi-segment rupture of the 2016 Amatrice-Visso-Norcia seismic sequence (central Italy) constrained by the first high-quality catalog of early aftershocks. *Sci. Rep.* **9**, 6921 (2019).

40. Michele, M., Chiaraluce, L., DiStefano, R. & Waldhauser, F. Fine-scale structure of the 2016–2017 central Italy seismic sequence from data recorded at the Italian national network. *J. Geophys. Res. Solid Earth* **125**, e2019JB018440 (2020).

41. Porreca, M. et al. 3D geological reconstruction of the M. Vettore seismogenic fault system (Central Apennines, Italy): Cross-cutting relationship with the M. Sibillini thrust. *J. Struct. Geol.* **131**, 103938 (2020).

42. Tondi, E. et al. The Campotosto linkage fault zone between the 2009 and 2016 seismic sequences of central Italy: Implications for seismic hazard analysis. *GSA Bull.* **133**, 1679–1694 (2020).

43. Waldhauser, F., Michele, M., Chiaraluce, L., DiStefano, R. & Schaff, D. P. Fault planes, fault zone structure and detachment fragmentation resolved with high-precision aftershock locations of the 2016–2017 central Italy sequence. *Geophys. Res. Lett.* **48**, 1–10 (2021).

44. Michele, M. et al. The Amatrice 2016 seismic sequence: A preliminary look at the mainshock and aftershocks distribution. *Ann. Geophysics* **59**, 1–8 (2016).

45. Vuan, A., Sugan, M., Chiaraluce, L. & Di Stefano, R. Loading rate variations along a midcrustal shear zone preceding the Mw 6.0 earthquake of 24 August 2016 in central Italy. *Geophys. Res. Lett.* **44**, 12170–12180 (2017).

46. De Luca, G., Cattaneo, M., Monachesi, G. & Amato, A. Seismicity in Central and Northern Apennines integrating the Italian national and regional networks. *Tectonophysics* **476**, 121–135 (2009).

47. Montuori, C. A., Murru, M., and Falcone, G. Spatial variation of the b-value observed for the periods preceding and following the 24 August 2016, Amatrice earthquake (ML6.0) (central Italy). *Ann. Geophys.* https://doi.org/10.4401/ag-7273 (2016).

48. Gulia, L. & Wiemer, S. Real-time discrimination of earthquake foreshocks and aftershocks. *Nature* **574**, 193–199 (2019).

49. García-Hernández, R., D'Auria, L., Barrancos, J., Padilla, G. D. & Pérez, N. M. Multiscale temporal and spatial estimation of the b-value. *Seismol. Res. Lett.* **92**, 3712–3724 (2021).

50. Tan, Y. J. et al. Machine-learning-based high-resolution earthquake catalog reveals how complex fault structures were activated during the 2016-2017 central Italy sequence. *Seismic Rec.* **1**, 11–19 (2021).

51. Suyehiro, S., Asada, T. & Ohtake, M. Foreshocks and aftershocks accompanying a perceptible earthquake in Central Japan. *Pap. Meteorol. Geophysics* **15**, 71–88 (1964).

52. Nanjo, K. Z., Hirata, N., Obara, K. & Kasahara, K. Decade-scale decrease in b value prior to the M9-class 2011 Tohoku and 2004 Sumatra quakes. *Geophys. Res. Lett.* **39**, 2012GL052997 (2012).

53. Tormann, T., Enescu, B., Woessner, J. & Wiemer, S. Randomness of megathrust earthquakes implied by rapid stress recovery after the Japan earthquake. *Nat. Geosci.* **8**, 152–158 (2015).

54. Nanjo, K. Z. & Yoshida, A. Anomalous decrease in relatively large shocks and increase in the p and b values preceding the April 16, 2016, M7.3 earthquake in Kumamoto, Japan. *Earth, Planets Space* **69**, 13 (2017).

55. Gulia, L. et al. The effect of a mainshock on the size distribution of the aftershocks. *Geophys. Res. Lett.* **45**, 13277–13287 (2018).

56. Chiaraluce, L. Unravelling the complexity of Apenninic extensional fault systems: A review of the 2009 L'Aquila earthquake (Central Apennines, Italy). *J. Struct. Geol.* **42**, 2–18 (2012).

57. Ciaccio, M. G. Instrumental seismicity of the Amatrice earthquake epicentral area: A review. *Ann. Geophysics* **59**, 1–8 (2016).

58. Moschella, M., Ciaccio, M. G. & Latorre, D. Minor earthquake sequences in the Amatrice-Norcia epicentral area (Central Italy). *Tectonophysics* **809**, 228858 (2021).

59. van der Elst, N. J. & Shaw, B. E. Larger aftershocks happen farther away: Nonseparability of magnitude and spatial distributions of aftershocks. *Geophys. Res. Lett.* **42**, 5771–5778 (2015).

60. Stallone, A. & Marzocchi, W. Empirical evaluation of the magnitude-independence assumption. *Geophys. J. Int.* **216**, 820–839 (2019).

61. Ellsworth, W. L. & Bulut, F. Nucleation of the 1999 Izmit earthquake by a triggered cascade of foreshocks. *Nat. Geosci.* https://doi.org/10.1038/s41561-018-0145-1 (2018).

62. Gomberg, J. Unsettled earthquake nucleation. *Nat. Geosci.* **11**, 463–464 (2018).

63. Segou, M. & Parsons, T. A new technique to calculate earthquake stress transfer and to probe the physics of aftershocks. *Bull. Seismological Soc. Am.* **110**, 863–873 (2020).

64. Mancini, S., Segou, M., Werner, M. J. & Parsons, T. The predictive skills of elastic Coulomb rate-and-state aftershock forecasts during the 2019 Ridgecrest, California, earthquake sequence. *Bull. Seismol. Soc. Am.* **110**, 1736–1751 (2020).

65. Hardebeck, J. L. Spatial clustering of aftershocks impacts the performance of physics-based earthquake forecasting models. *J. Geophys. Res. Solid Earth* **126**, e2020JB020824 (2021).

66. Grünthal, G., Wahlström, R. & Stromeyer, D. The unified catalogue of earthquakes in central, northern, and northwestern Europe (CENEC)—Updated and expanded to the last millennium. *J. Seismol.* **13**, 517–541 (2009).

67. Piegari, E., Herrmann, M. & Marzocchi, W. 3-D spatial cluster analysis of seismic sequences through density-based algorithms. *Geophys. J. Int.* **230**, 2073–2088 (2022).

68. Ester, M., Kriegel, H.-P., Sander, J. & Xu, X. In *Proceedings of the 2nd International Conference on Knowledge Discovery and Data Mining (KDD-96)* (eds. Simoudis, E et al.) 226–231 (AAAI Press, 1996).

69. Kagan, Y. Y. Short-term properties of earthquake catalogs and models of earthquake source. *Bull. Seismol. Soc. Am.* **94**, 1207–1228 (2004).

70. Helmstetter, A., Kagan, Y. Y. & Jackson, D. D. Comparison of short-term and time-dependent earthquake forecast models for southern California. *Bull. Seismol. Soc. Am.* **96**, 90–106 (2006).

71. Hainzl, S. Apparent triggering function of aftershocks resulting from rate-dependent incompleteness of earthquake catalogs. *J. Geophys. Res. Solid Earth* **121**, 6499–6509 (2016).

72. de Arcangelis, L., Godano, C. & Lippiello, E. The overlap of aftershock coda waves and short-term postseismic forecasting. *J. Geophys. Res. Solid Earth* **123**, 5661–5674 (2018).

73. Agnew, D. C. Equalized plot scales for exploring seismicity data. *Seismol. Res. Lett.* **86**, 1412–1423 (2015).

74. Tinti, S. & Mulargia, F. Confidence intervals of b values for grouped magnitudes. *Bull. Seismol. Soc. Am.* **77**, 2125–2134 (1987).

75. Herrmann, M. & Marzocchi, W. Mc-Lilliefors: A completeness magnitude that complies with the exponential-like Gutenberg–Richter relation. *Zenodo* https://doi.org/10.5281/zenodo.4162497 (2020).

76. Lolli, B., Randazzo, D., Vannucci, G. & Gasperini, P. The Homogenized Instrumental Seismic Catalog (HORUS) of Italy from 1960 to present. *Seismol. Res. Lett.* **91**, 3208–3222 (2020).

77. Gasperini, P., Lolli, B. & Vannucci, G. Empirical calibration of local magnitude data sets versus moment magnitude in Italy. *Bull. Seismol. Soc. Am.* **103**, 2227–2246 (2013).

78. Tan, Y. J., Waldhauser, F. & Ellsworth, W. L. Machine-learning-based high-resolution earthquake catalog for the 2016–2017 Central Italy sequence. *Zenodo* https://doi.org/10.5281/zenodo.4662870 (2021).

Author contributions

M.H. performed the statistical analyses, created the figures, and wrote the manuscript. E.P. performed the clustering analysis and reviewed the manuscript. W.M. outlined and led the project and reviewed the manuscript. All authors designed the study and discussed the results.

Competing interests

The authors declare no competing interests.

Additional information

Supplementary information The online version contains supplementary material available at https://doi.org/10.1038/s41467-022-32755-6.

Correspondence and requests for materials should be addressed to Marcus Herrmann.

Peer review information *Nature Communications* thanks the anonymous, reviewer(s) for their contribution to the peer review of this work. Peer reviewer reports are available.

Reprints and permission information is available at http://www.nature.com/reprints

Publisher's note Springer Nature remains neutral with regard to jurisdictional claims in published maps and institutional affiliations.